npj | parkinson's disease

Article

Published in partnership with the Parkinson's Foundation

https://doi.org/10.1038/s41531-025-00989-y

A new *LRRK2* variant in a family with Parkinson's disease affects binding to RAB8A

Lydia Vela-Desojo[1], Alba Pascual[2,3], Victor Montal[4], Carmen Guerrero[5], Mireia Osuna-López[2], Victor Guallar[4,6], Francesc Palau[2,3,7,8,9] & Janet Hoenicka[2,3,9] ✉

Pathogenic variants in the *LRRK2* gene affecting catalytic domains are the most common genetic cause of Parkinson's disease (PD). Nevertheless, *LRRK2* variants at the armadillo (ARM) domain would indirectly affect the protein's activity by interacting with RAB proteins. We present a family with PD recurrence segregating the new *LRRK2* allele at the ARM domain, p.[Leu.119Pro;Leu488Pro]. Clinical exams were conducted on nine relatives. Neuropathology of the index case showed loss of substantia nigra neurons and Alzheimer's disease-type lesions. In silico analysis of the p.[Leu.119Pro;Leu488Pro] *LRRK2* variant predicted alterations in ARM tertiary structure and binding affinity. These predictions were supported by functional genomics using recombinant $LRRK2^{WT}$ and $LRRK2^{Leu119Pro;Leu488Pro}$. We found increased interaction between $LRRK2^{Leu119Pro;Leu488Pro}$ and RAB8A, but not with RAB10. Additionally, docking studies revealed stronger affinity of $LRRK2^{Leu119Pro;Leu488Pro}$ for RAB8A ($P < 0.0001$) and allosteric properties beyond the mutated residues. We propose p.[Leu119Pro;Leu488Pro] as a cause of familial PD.

Pathogenic missense variants in the leucine-rich repeat kinase 2 (*LRRK2*) gene are the most common genetic cause of familial and sporadic Parkinson's disease (PD)[1]. Most PD-causing *LRRK2* variations are clustered in the kinase and Roc-COR enzymatic domains. All these variants increase the LRRK2 kinase activity either directly or by compromising the GTPase function[2]. In addition, genetic variants of *LRRK2* affecting scaffold domains of the protein have been identified as risk or protective factors for PD in different populations[3].

The most well-validated physiological LRRK2 substrates are a subset of RAB proteins, which are small GTPases that regulate the secretory and endocytic pathways[4,5]. LRRK2 interacts with and phosphorylates RAB proteins through its armadillo (ARM) domain to regulate their activities, localisation, and effector binding[6,7]. In turn, RAB proteins phosphorylated by LRRK2 bind to its ARM domain, creating a feed-forward pathway that provides spatial control and activates LRRK2 kinase activity[8]. Therefore, *LRRK2* missense variants located at the ARM domain would indirectly affect the kinase activity of the protein[9,10].

Here, we present a family with a high recurrence of PD and the new *LRRK2* variant p.[Leu119Pro;Leu488Pro] segregating with the disease, which is located in the ARM domain. This multidisciplinary study includes the family's clinical, pathological, and genetic characterisation, as well as computational and experimental investigations to validate the impact of p.[Leu119Pro;Leu488Pro]. We provide evidence of the pathogenicity of this novel *LRRK2* allele using both cellular models and docking studies, which suggested that p.[Leu119Pro;Leu488Pro] increases LRRK2 binding to RAB8A.

Results

Clinical and genetic findings

The index case (II-6) had a substantial family history with the father affected by PD and, later on, two brothers and a nephew (Fig. 1a). She was 57 years old when PD was diagnosed. Resting tremor (RT) in her right limbs was the first symptom. She had a good response to levodopa-carbidopa (LDCD), but seven years later, she developed dyskinesias and motor fluctuations. She does not have orthostatic hypotension or early urinary problems. Because

[1]Movement Disorders Unit, Department of Neurology, Hospital Universitario Fundación Alcorcón, Madrid, Spain. [2]Laboratory of Neurogenetics and Molecular Medicine, Institut de Recerca Sant Joan de Déu, Barcelona, Spain. [3]Centro de Investigación Biomédica en Red de Enfermedades Raras (CIBERER), ISCIII, Madrid, Spain. [4]Barcelona Supercomputing Center, Barcelona, Spain. [5]Department of Pathology, Hospital Fundación Alcorcon, Madrid, Spain. [6]Nostrum Biodiscovery, Barcelona, Spain. [7]Únicas SJD, Hospital Sant Joan de Déu, Barcelona, Spain. [8]Division of Pediatrics, University of Barcelona School of Medicine and Health Sciences, Barcelona, Spain. [9]These authors contributed equally: Francesc Palau, Janet Hoenicka.
✉e-mail: janet.hoenicka@sjd.es

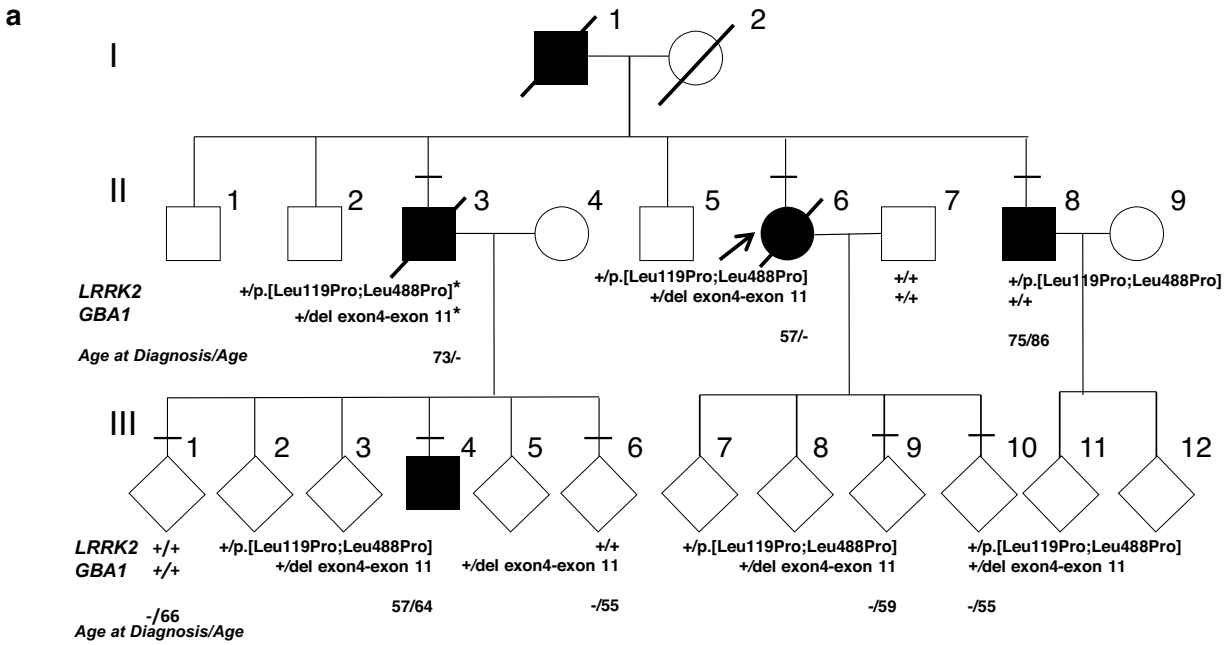

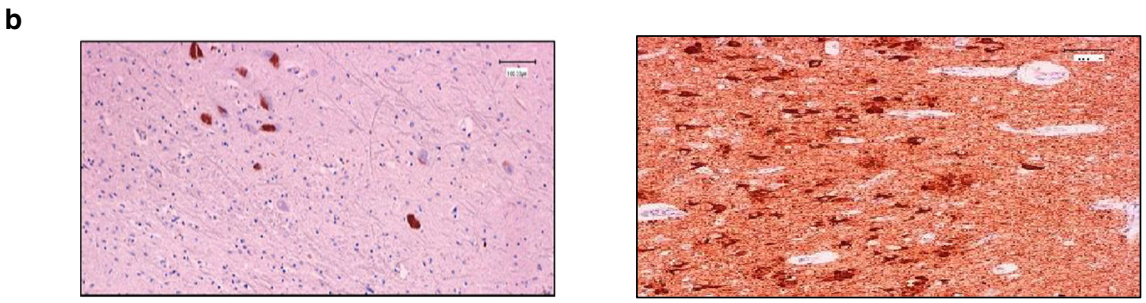

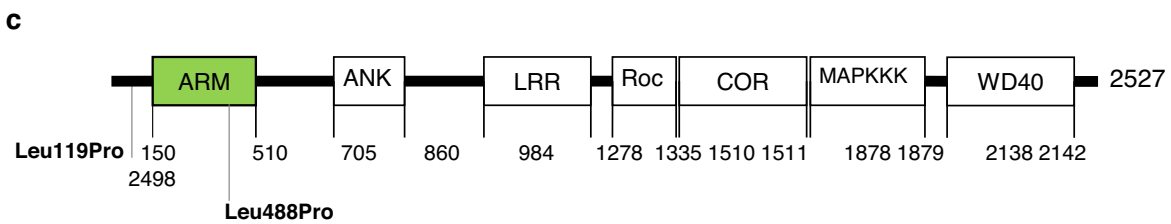

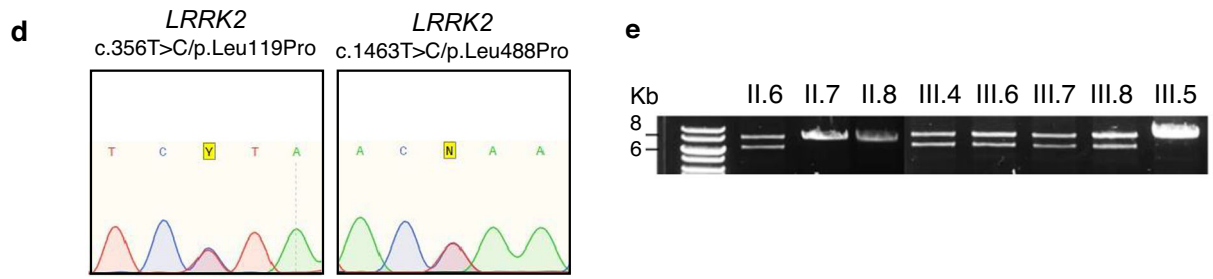

oral medication could not control levodopa-induced complications, LDCD intestinal gel infusion (DUODOPA®, AbbVie) was started when she was 79 years old. At that time, off-medication UPDRS part III scored 38 with a Hoehn–Yahr (H&Y) stage of 3. This treatment resulted in much improvement in her quality of life. At 83, cognitive assessment using the SCales for Outcomes in Parkinson's disease-COGnition (SCOPA-COG) scored 21/43 (score range: 0–43, higher scores reflecting better performance). Cognitive impairment progressed until she died at 86.

Her brain was donated to the Hospital Fundación Alcorcon Brain Bank. Moderate cortical atrophy was observed at autopsy, being more intense in the middle gyrus of the frontal lobe and the *operculum*. The ventricular system showed mild dilatation in coronal sections of the

Fig. 1 | Family tree, neuropathology and molecular findings of the PD family related to the novel *LRRK2* allele p.[Leu119Pro; Leu488Pro] and *GBA1* deletion. **a** The family tree of the patients depicts the family history of PD. Squares symbolise males and circles females. All filled squares/circles indicate affected members, and the line above squares/circles indicates neurological assessment. *LRRK2* and *GBA* genotypes are indicated. Age at diagnosis and current age are below the genotypes. The asterisk indicates an obligatory carrier (individual II.3). **b** Neuropathology of the index case: substantia nigra showed no Lewy bodies or neurites after immunostained with α-alpha-Synuclein (left). Hippocampus neurofibrillary tangles and neuropilic threads after immunostaining with α-Tau (AT 100) (right). Images were taken from optical sections that are representative of the group averages. Scale bar: 100 µm. **c** LRRK2 domains structure and the location of p.[Leu119Pro;Leu488Pro]. ARM: armadillo repeats, ANK: ankyrin repeats, LRR: leucine-rich repeats, Roc: Ras of complex proteins, COR: C-terminal of ROC, MAPKKK: kinase domain, WD40: WD40 repeats. **d** Sanger sequencing *LRRK2* p.[Leu119Pro; Leu488Pro] chromatogram. Right: *LRRK2* p.Leu488Pro/c.1463 T > C variant and left *LRRK2* p.Leu119-Pro/c.356 T > C variant. **e** *GBA1* long PCR amplicons showing the deletion in the carriers.

Table 1 | Clinical and genotype data from affected and unaffected members of the Parkinson's family

FAMILY MEMBER	AGE AT DIAGNOSIS	YEARS OF EVOLUTION	RT	MF	D	PS	CI	NI	GENETIC FINDINGS
II.6 (†)	57	29	Yes	Yes	Yes	Yes[&]	Mild dementia	DaTSCAN[Ω] MRI: normal	*LRRK2*: p.[Leu119Pro; p.Leu488Pro] *GBA1*: del exon4-exon 11
II.3 (†)	73	14	Yes	No	No	–	Dementia	–	*
II.7	NA	NA	No	No	No	No	NA	–	None
II.8	75	11	Yes	No	No	No	No	DaTSCAN[Ω]	*LRRK2*: p.[Leu119Pro; p.Leu488Pro]
III.4	57	7	Yes	Yes	Yes	Yes	Mild Cognitive Impairment	DaTSCAN[Ω] MRI[Ω]	*LRRK2*: p.[Leu119Pro; p.Leu488Pro] *GBA1*: del exon4-exon 11
III.1	NA	NA	No	No	No	No	NA	–	None
III.6	NA	NA	No	No	No	No	NA	–	*GBA1*: del exon4-exon 11
III.9	NA	NA	No	No	No	No	NA	–	*LRRK2*: p.[Leu119Pro; p.Leu488Pro] *GBA1*: del exon4-exon 11
III.10	NA	NA	No	No	No	No	NA	–	*LRRK2*: p.[Leu119Pro; p.Leu488Pro] *GBA1*: del exon4-exon 11

NA not applicable, *RT* resting tremor, *MF* motor fluctuation, *D* Dyskinesias, *PS* psychotic symptoms, *NI* neuroimaging studies, *DaTScan* single photon emission computed tomography with Ioflupane I123 injection, *DaTScan*[Ω] showed a decrease in the uptake of the radiotracer in the putamen, *MRI* magnetic resonance imaging, *MRI*[Ω] small hyperintense lesions in white matter
[&]After pharmacological treatment *CI* cognitive impairment
[*]Obligatory carrier of *LRRK2*: p.[Leu.119Pro; p.Leu488Pro] and *GBA*: del exon4-exon 11

cerebrum. No other cerebral alterations were observed except for a sieve-like state in the white matter and the basal ganglia. There was pallor of the *substantia nigra* (SN) and the *locus ceruleus* (LC) (Fig. S1a). Axial sections of the brainstem showed mild atrophy. The cerebellum showed no abnormality.

The main microscopic findings were observed in the SN with substantial loss of dopaminergic neurons and gliosis (Fig. S1a). Neuronal loss in the locus coeruleus was less intense. Intense astrocytosis was observed in the rest of the subcortical grey nuclei. Lewy bodies were not observed in any part of the brain. There was slight transcortical gliosis in cortical grey matter and patchy laminar microvacuolization in cortical layers II and III. Inmunohistochemistry using α-AT100 and α-beta-amyloide (Aβ) showed Alzheimer's Disease Neuropathologic Changes, with neurofibrillary tangles (NFTs) and senile plaques ranked in A2, B2, C2 score[11] (Figs. 1b and S1b, c). NFTs were noticed in the entorhinal cortex, closely related areas, and the hippocampus, corresponding to Braak stages III/IV. In addition, the hippocampus showed patchy neuronal loss, slight gliosis, mixed 3R and 4R Tau, granule-vacuolar degeneration and Hirano bodies. There were no immunoreactive inclusions with α-TAR-DNA-binding protein (TDP-43) or α-synuclein. These neuropathological findings force us to rule out a genetic PD.

Genetic analysis of the patient (II-6) using a custom NGS targeted panel detected two heterozygous rare single-nucleotide variants (SNVs) in the *LRRK2* gene (Tables 1 and S1). The variants were aminoacidic non-conservative changes of leucine by proline at positions 119 (c.356 T > C/p.Leu119Pro, rs33995463) and 488 (c.1463 T > C/p.Leu488Pro, novel variant) (Fig. 1c). The 2 SNVs were confirmed by Sanger sequencing (Fig. 1d). p.Leu119Pro and p.Leu488Pro are located at the ARM domain (IPR016024) in evolutionary conserve positions (Fig. S2). These SNVs are rare in all populations (Table S2). To assess the frequency of these changes in populations of PD patients, we used data from the Accelerating Medicines Partnership Parkinson's Disease (AMP-PD) group[12]. We found that p.Leu119Pro occurred with a frequency of 0.59 (17 alleles out of 2835), while p.Leu488Pro was not present in this population. Additionally, conflicting interpretations of pathogenicity were obtained using different baseline criteria (Tables S2 and S3 and Fig. S3). Due to the patient's neuropathological findings, we interrogated genes for disorders with Tau pathology using a clinical exome sequencing (CES) panel (Table S4). No pathogenic variants were found in any of the genes.

The index case nephew (III-4) was 57-years-old when RT in his right limb started. PD was diagnosed with an excellent response to LDCD, but dyskinesias and motor fluctuations developed four years after the diagnosis. When we saw the patient, off-medication UPDRS part III scored 40, and he had a stage 3 of H&Y. Because of uncontrolled motor complications, he was treated with deep brain stimulation in both subthalamic nuclei. Dyskinesia and motor fluctuations improved greatly, but dysarthria and gait freezing did not. Mild cognitive impairment was present since he was 62-years-old. Genetic analysis revealed that this patient was a carrier of both variants in *LRRK2*. The index's brother (II-8) developed PD at an older age and did not experience severe motor complications or cognitive decline.

As we found evidence of a β-Glucocerebrosidase (*GBA1*) gene gross deletion in II-6 and III-4 patients' samples, we amplified the entire *GBA1*

gene using long-PCR as previously described. Both patients had a two-band pattern corresponding to the *GBA1* gene (8 Kb) and a smaller band of 6 Kb. Patient (II-8) did not carry the *GBA1* deletion (Fig. 1e).

Sanger sequencing of the smaller band revealed a recombination event of *GBA1* with its pseudogene *GBAP1*. In addition, we located the 5' recombination point by Sanger sequencing; the breaking point localised at the intron 2/10 of the *GBA1* gene in a thymine repeat area (Fig. S4). Since exon 11 of the *GBA1* and *GBAP1* genes are nearly identical, we could not detect the downstream recombination point. Nevertheless, we identified *GBAP1* exon 11 and the rs421016, rs368060 and rs1135675 SNVs in exon ten found in *GBAP1* (Fig. S4).

Genetic testing by Sanger sequencing was performed after written informed consent in 6 additional relatives of the PD index case. They were patient II-8, four at-risk asymptomatic individuals (children III-9, 59-years-old, and III-10, 55-years-old), and the brother's children (III-1, 66-years-old, and III-6, 55-years-old), and her unaffected husband (II-7). Table 1 shows clinical features and the genetic results. The affected brother (II-8) carried the *LRRK2* SNVs. The two probands' children were carriers of the *LRRK2* SNVs and the *GBA1* deletion. This segregation analysis confirmed that p.[Leu119Pro; Leu488Pro] are in *cis*. On the other hand, the two brothers' children were not carriers of *LRRK2* SNVs, but did carry other variants, including *GBA1* deletion in III-1. Thus, genetic testing showed that all affected relatives were carriers of p.[Leu119Pro;Leu488Pro], while some asymptomatic relatives carried all or one of the rare variants found in the index case. These findings suggest that p.[Leu119Pro; Leu488Pro] in *LRRK2* is not fully penetrant in this family, at least in individuals younger than 60.

In silico and in vitro studies

Our in silico studies, based on the experimental structure of LRRK2 (PDB:8FO2), indicate that the p.[Leu119Pro; Leu488Pro] variant alters the secondary structure of LRRK2 (Fig. S3a). Using various tools of PyMOL (version 1.8)[13], the analysis revealed slight differences in structural flexibility, leading to reduced atomic mobility (greater rigidity) and slight changes in the electrostatic potential surfaces between $LRRK2^{WT}$ and $LRRK2^{Leu119Pro;Leu488Pro}$ (Fig. S3b, c). DynaMut2[14] and DUET evaluated the impact of mutations on protein stability, predicted considerable deleterious effects for the p.[Leu119Pro;Leu488Pro] variant, with notable changes in folding free energy ($\Delta\Delta G_{\text{Leu119-Leu488} \rightarrow \text{Pro119-Pro488}}$ STABILITY: −1.89 Kcal/mol and −1.39 Kcal/mol, respectively) and increased protein instability (Fig. S3d). Additionally, Missense3D predicted structural damage due to introducing a buried proline and the buried/exposed switch, where the substitution caused a shift between the buried and exposed states of the target residue (Fig. S3d). SPPIDER further predicted the creation of new binding sites near position 119 and the loss of binding sites near position 488 in $LRRK2^{Leu119Pro;Leu488Pro}$ (Fig. S3e). Collectively, these in silico findings, combined with the low frequency of these SNVs would support the notion that the p.[Leu119Pro;-Leu488Pro] allele is pathogenic.

We then performed experimental studies by overexpressing in HEK293 cells pDEST53-$LRRK2^{WT}$ and pDEST53-$LRRK2^{Leu119Pro;Leu488Pro}$ constructs (obtained by mutagenesis of the former). The two constructs express the *LRRK2* open reading frame in fusion with the green fluorescence protein (GFP). We observed that recombinant LRRK2 localised in the cytoplasm homogeneously or formed aggregates. We found no allele-dependent differences in the expression pattern of the recombinant proteins (Fig. 2a). Since the ARM domain of LRRK2 interacts with RAB proteins[15], we studied the effect of p.[Leu119Pro; Leu488Pro] upon this interaction. RAB10 and RAB8A were selected as candidates because they are well-characterised and there is evidence of their interaction with the ARM domain of LRRK2[8]. Using proximity ligation assay (PLA), we quantified the interaction between recombinant $LRRK2^{WT}$ or $LRRK2^{Leu119Pro;Leu488Pro}$ with endogenous RAB10 or RAB8A. PLAs results revealed no differences between $LRRK2^{WT}$ or $LRRK2^{Leu119Pro;Leu488Pro}$ in their interaction with RAB10 ($P = 0.4192$) (Fig. 2b). When we tested the interaction with RAB8A, we found a significant increase in the number of interactions per cell for $LRRK2^{Leu119Pro;Leu488Pro}$ and RAB8A compared to $LRRK2^{WT}$ ($P < 0.0001$) (Fig. 2c). These results suggest that the LRRK2 variant p.[Leu119Pro;-Leu488Pro] has differential effects on its substrates RAB8A and RAB10.

p.[Leu119Pro; Leu488Pro] increases potential docking poses and binding affinity between LRRK2 and RAB8A

To further investigate the effect of p.[Leu119Pro; Leu488Pro] on LRRK2 and its binding affinity for RAB8A and RAB10, we conducted a docking study. We first used Masif to compute, for each residue at the LRRK2 surface, its probability of being part of a protein–protein interface. For residue 119 of LRRK2, we found that Leu had a lower probability score than Pro (0.41 vs 0.55, respectively). At residue 488, we found a low score for both Leu and Pro (0.24 vs 0.20, respectively), suggesting that this residue does not participate in the LRRK2-RAB8A/RAB10 complex interface.

To gain more insight into the protein–protein interface of LRRK2 in the region affected by p.[Leu119Pro;Leu488Pro] we used PyDock. We focused on the top 100 and 1000 pyDock poses to minimise the bias of false-positive docking poses. When evaluating the docking results for LRRK2-RAB8A (structure representation of the top energetic pose of the complex in Fig. 3a), the poses close to residue 119 showed increased number of docking poses for $LRRK2^{Leu119Pro;Leu488Pro}$ (10/100 and 101/1000) compared to $LRRK2^{WT}$ (6/100 and 76/1000) (Fig. 3b, left). No pose was found close to residue 488 for either $LRRK2^{WT}$ or $LRRK2^{Leu119Pro;Leu488Pro}$. Importantly, we observe larger number of docking poses close to residue 301 (residue at top pyDock pose) for $LRRK2^{Leu119Pro;Leu488Pro}$ (89/100 and 453/1000) compared to $LRRK2^{WT}$ (59/100 and 453/1000), suggesting a potential allosteric effect on the LRRK2 structure in regions beyond the mutated residues. In this regard, the Masif probability score at residue 301 increased from 0.42 in $LRRK2^{WT}$ to 0.48 in $LRRK2^{Leu119Pro;Leu488Pro}$. Notably, the number of pyDock poses close to residues 119 and 301 for the LRRK2–RAB10 system was systematically lower, proposing a lower affinity of RAB10 in those two regions (Fig. 3b, right).

To optimise the complex poses around LRRK2 residues 119 and 301 and obtain an energetic binding energy score, we used PELE[16]. For the pose close to residue 119, we found that $LRRK2^{Leu119Pro;Leu488Pro}$ had a lower binding energy to RAB8A (more affinity) compared to $LRRK2^{WT}$ (−84.1 kcal/mol vs −77.2 kcal/mol, respectively). This difference was even more marked at residue 301, in which $LRRK2^{Leu119Pro;Leu488Pro}$ presented the lowest binding energy of −87.8 kcal/mol, compared to the -65 kcal/mol of $LRRK2^{WT}$ pose (Fig. 3c, left). These results suggest that p.[Leu119Pro;-Leu488Pro] has an effect of increased interaction both locally (at residue 119) and allosterically (at residue 301). We did not explore the pose close to residue 488 due to no available pose within the top 1000 pyDock poses. In contrast, $LRRK2^{Leu119Pro;Leu488Pro}$-RAB10 showed higher binding energy (lower affinity) for the pose close to residue 119, compared to $LRRK2^{WT}$. We noticed that for the pose close to residue 301, the $LRRK2^{Leu119Pro;Leu488Pro}$–RAB10 system showed lower binding energy. Nevertheless, we hypothesise that this difference would be negligible, given the low number of poses identified in the pyDock analysis.

We then used steered molecular dynamics to capture how p.[Leu119Pro;Leu488Pro] affect the force required to break the binding between LRRK2 and RAB8A (Fig. 3d, left). The average peak force to separate RAB8A from $LRRK2^{Leu119Pro;Leu488Pro}$ was ~1600 kJ/mol nm^2, which is higher than for $LRRK2^{WT}$ (~ 1250 kJ/mol nm^2) close to residue 119. Similarly, the peak dissociation force at the position near residue 301 was higher for $LRRK2^{Leu119Pro;Leu488Pro}$ (~1500 kJ/mol nm^2) compared to $LRRK2^{WT}$ (~1100 kJ/mol nm^2). These results further verify a stronger affinity between $LRRK2^{Leu119Pro;Leu488Pro}$ and RAB8A, compared to $LRRK2^{WT}$. RAB10 analyses showed an increase in the pulling force required for $LRRK2^{Leu119Pro;Leu488Pro}$ compared to $LRRK2^{WT}$ at the pyDock pose near residue 119 (difference of 350 kJ/mol nm^2 for RAB8A vs ~300 kJ/mol nm^2 for RAB10). However, this difference was marginal at the pyDock energy maxima position (Fig. 3c, right). Despite the force differences at residue 119, we consider that it will have a residual impact on the overall binding of LRRK2–RAB10, given the low number of PyDock poses.

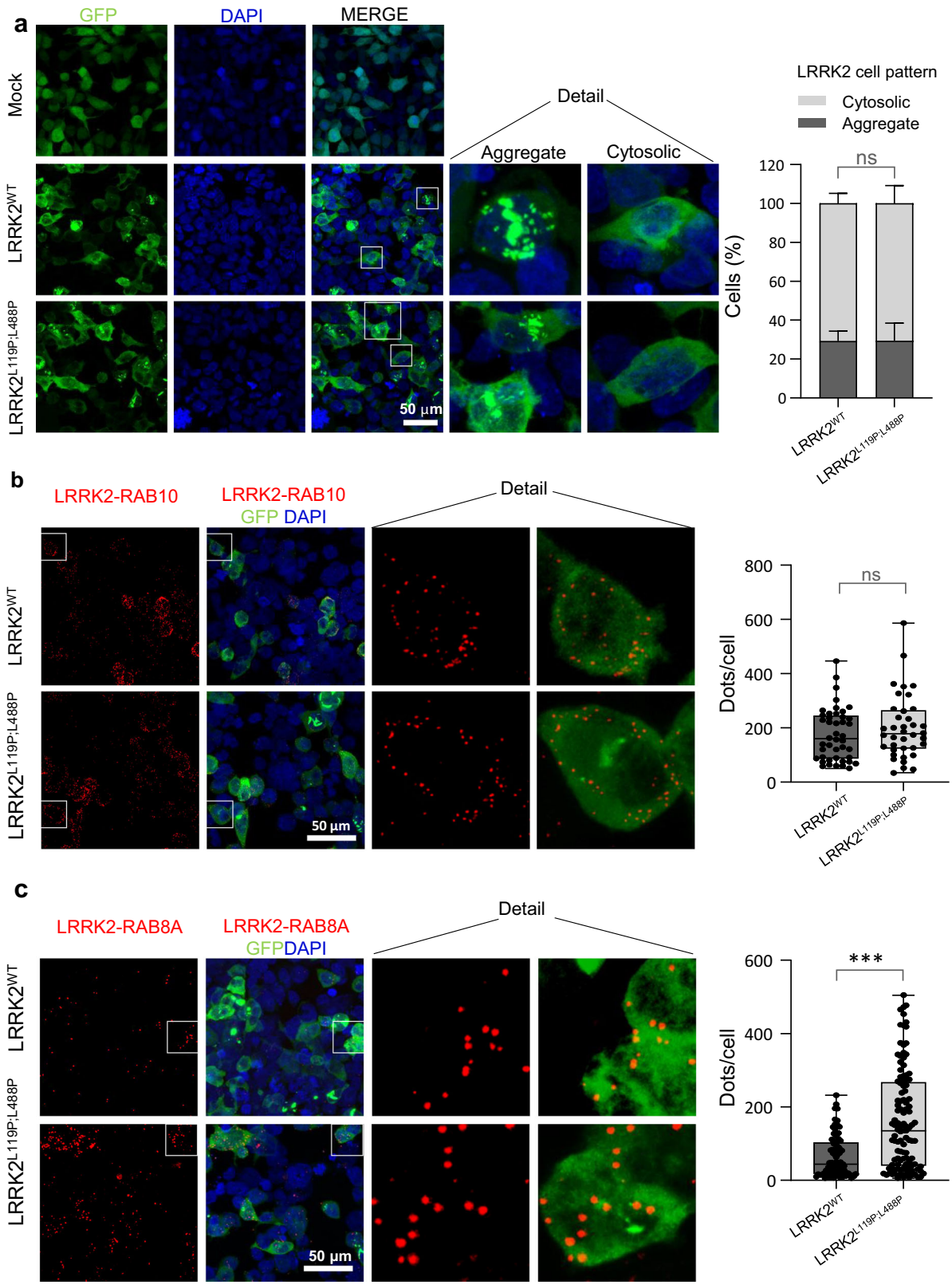

Fig. 2 | Functional genomics study of recombinant LRRK2^{WT} and LRRK2$^{Leu119Pro;Leu488Pro}$ shows increased binding to RAB8A. a Representative images of recombinant LRRK2 proteins in fusion with GFP (left) and signal quantification for cytosolic or aggregate patterns. LRRK2^{WT}: 70.78 ± 5.11 cytosolic and 29.22 ± 5.11 aggregate vs LRRK2$^{Leu119Pro;Leu488Pro}$ 70.58 ± 9.17 cytosolic and 29.42 ± 9.17 aggregate (Four independent experiments, at least 30 cells). Cochran–Mantel–Haenszel χ^2 test: *P*-value = 0.9975 **b** Representative images of proximity ligation assays using α-GFP (LRRK2^{WT} and LRRK2$^{Leu119Pro;Leu488Pro}$) and α-RAB10. On the right is the quantification of the interaction number of LRRK2-RAB10 (dots) per cell. **c** Representative images of proximity ligation assays using α-GFP (LRRK2^{WT} and LRRK2$^{Leu119Pro;Leu488Pro}$) and α-RAB8A. On the right, quantification of the interaction number of LRRK2-RAB8A (dots) per cell. **b**, **c** The box plot lines correspond from the bottom of the box to the top: 25th percentile, median, 75th percentile. The whiskers extend to the minimum and maximum values. Three independent experiments with four different images for each experiment. Shapiro test followed by Mann–Whitney *U*-test: ns not significant, ****P*-value < 0.001.

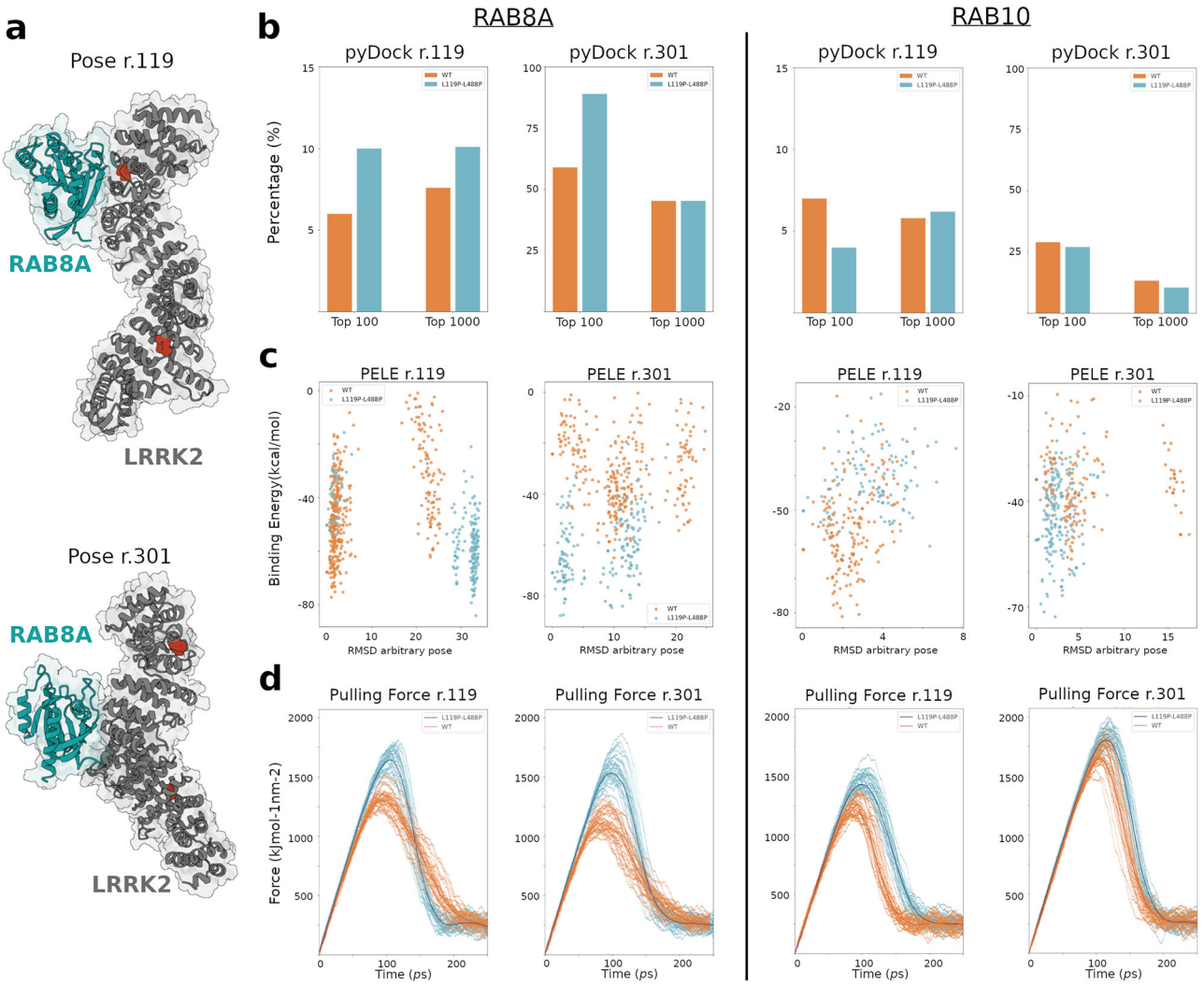

Fig. 3 | Comparison of the effect of p.[Leu119Pro;Leu488Pro] on the interaction affinity of LRRK2-RAB8A or LRRK2-RAB10. a Structural representation of the top energetic pose of the complex between LRRK2 (grey) and RAB8A (cyan), close to LRRK2 residues 119 (TOP) and 301-top pyDock (BOTTOM). The red dots highlight p.Leu119Pro and p.Leu488Pro LRRK2 SNVs. **b** Percentage of poses obtained from pyDock regarding RAB8A (left) and RAB10 (right) close to LRRK2 residues 119 and 301, for LRRK2^{WT} (orange) and LRRK2$^{Leu119Pro;Leu488Pro}$ (blue). **c** Binding energy profiles obtained from PELE for poses regarding RAB8A (left) and RAB10 (right) close to LRRK2 residues 119 and 301 for LRRK2^{WT} (orange) and LRRK2$^{Leu119Pro;Leu488Pro}$ (blue). **d** Steering MD results representing the pulling force for the LRRK2-RAB complex regarding RAB8A (left) and RAB10 (right) close to LRRK2 residues 119 and 301, for LRRK2^{WT} (orange) and LRRK2$^{Leu119Pro;Leu488Pro}$ (blue).

Discussion

This study identified the novel *LRRK2* variant allele p.[Leu119Pro;Leu488Pro], which affects the ARM domain, in a family with autosomal dominant PD. We further provided evidence of how this variant, located far from the catalytic domains of LRRK2, may cause the disease.

The pathophysiology of PD caused by *LRRK2* variants in the catalytic domains is attributed to a gain of kinase function leading to hyperphosphorylation of substrates[2]. More recently, LRRK2 variants located at the scaffold ARM domain have been reported to cause an increase in LRRK2 kinase activity as well[9,17]. Indeed, the LRRK2 ARM domain is involved in the dimeric structure of the holoenzyme, which is needed for its kinase activity[18]. Therefore, evidence indicates that the LRRK2 ARM domain contributes to its kinase activity, and mutations in this domain may increase the potentially toxic function of the mutated protein. Regarding p.[Leu119Pro;Leu488Pro], this variant consists of two Leu-to-Pro substitutions at conserved positions of the ARM domain of LRRK2 that could affect the tertiary structure and change the binding affinity of LRRK2 and its partners. Our experimental results with recombinant LRRK2^{WT} and LRRK2$^{Leu119Pro;Leu488Pro}$ proteins supported these predictions, indicating significant differences in their interactions with RAB8A, although this did not occur with RAB10. It could be proposed that p.[Leu119Pro;Leu488Pro] may specifically increase the interaction between LRRK2 and RAB8A, or affect the phosphorylation levels of RAB8A. Previous research has reported *LRRK2* variant differences upon phosphorylation of RAB10 vs RAB12, suggesting pathophysiological variations among LRRK2 variants[19].

RAB8A is linked to PINK1[20] and α-Synuclein[21], PD-related proteins involved in dysfunctional mitochondrial dynamics and mitophagy. On the lysosomal side, although both RAB8A and RAB10 respond to lysosomal damage[22–24], very recently these RAB proteins have been shown to have opposite roles in lysosomal biology[25]. These functional differences between RAB8A and RAB10 could be related to the increased interaction of LRRK2$^{Leu119Pro;Leu488Pro}$ with RAB8A and not RAB10.

From a three-dimensional viewpoint, our docking studies revealed a substantial increment in the affinity of LRRK2 ARM domain for RAB8A in the presence of p.[Leu119Pro; Leu488Pro] ($P < 0.0001$). This change in the affinity is attributed to both mutations together; however, the differential local effects were observed exclusively at residue 119. Of note, the allele *LRRK2*:p.Leu119Pro is overrepresented in Spanish patient cohorts and

absent in both a Spanish control population[26] and a clinical series of 105 early-onset PD patients (unpublished results). Furthermore, p.[Leu119Pro; Leu488Pro] may exhibit allosteric properties that influence LRRK2 structure in areas beyond the mutated residues, suggesting that this double variant allele could have a more pronounced effect on LRRK2 than p.Leu119Pro alone. Overall, our docking findings show that $LRRK2^{Leu119Pro;Leu488Pro}$ has a higher affinity for RAB8A, which may lead to a gain of function in LRRK2 and contribute to the disease expression. Moreover, our computational results also highlight the lack of effect on RAB10, which agrees with our PLA analyses.

We also found that the index case was heterozygous for a previously reported *GBA1* gross deletion[27] that we detected in II-6 and III-4 patients. This heterozygous *GBA1* deletion may impact clinical progression, as carriers of the *GBA1*-deleted allele frequently exhibit cognitive impairment. In contrast, patient II-8, who is not a carrier of this variant, showed a milder disease progression. It is important to note that we found unaffected relatives under the age of 60 who carry p.[Leu119Pro; Leu488Pro]. They are the children of the index case whose current clinical examination reveals no considerable findings. Given the age-related penetrance of other *LRRK2* variants, we propose that these would be asymptomatic carriers from whom we should follow up clinically. Finally, we found that Lewy bodies were absent in the index case, while AD-type tau lesions and amyloid plaques were present. This finding aligns with *LRRK2*-related pathology. On the one hand, 21–54% of PD cases with variants in *LRRK2* do not present Lewy bodies; on the other hand, prominent AD-type tau pathology is observed in most of the brains of *LRRK2*-PD cases[28].

A limitation of our study is the relatively small size of the family and the limited number of available meioses to statistically evaluate the pathogenicity of the *LRRK2* and *GBA1* variants within this family. Consequently, we could not reach sufficient LOD score values to confirm the linkage between PD and the *LRRK2* variant allele. Nevertheless, we performed a comprehensive study combining clinical, genetic, functional genomics, and computational analyses. These approaches suggest the pathogenicity of p.[Leu119Pro;Leu488Pro]. Additionally, we focused our computational and functional studies on evaluating the differences between $LRRK2^{WT}$ and $LRRK2^{Leu119Pro;Leu488Pro}$ proteins. The biology of RAB proteins and their biochemical pathways has been studied in relation to their interaction with LRRK2. Further biochemical analysis of RAB proteins requires additional experiments. Still, this study deserves attention for its focus on rare variants affecting the ARM region of LRRK2 and their differential impact on interactions with RAB proteins.

In summary, we have identified and studied the novel *LRRK2* variant p.[Leu119Pro; Leu488Pro], which we propose as a cause of familial PD. Further studies about the impact of other *LRRK2* ARM domain disease-causing variants are of major interest now and will also be for therapeutic decision-making in precision medicine.

Methods

Clinical and neuropathological exams

We studied a Spanish Caucasian family with a known history of Parkinsonism in five members from three generations, segregating in an autosomal dominant manner. Neurological examination was performed in the Movement Disorders Clinic at the Hospital Fundacion Alcorcon in Madrid (Spain). Diagnosis of PD was made based on London Brain Bank criteria[29]. Clinical examinations of PD patients included the Unified Parkinson's Disease Rating Scale (UPDRS)[30], Hoehn & Yahr scale[31] and cognitive assessment according to the Movement Disorders Society Task Force on PD dementia[32]. The study received approval from the Hospital's Ethics Committees, and informed consent was obtained from all participants whose genomic DNA was analysed (PIC-217-19).

Neuropathological autopsy and microscopy studies of the index case were performed in formalin-fixed and paraffin-embedded blocks of the cerebral cortex and white matter, basal ganglia, midbrain, brain stem, and cerebellar cortex. Immunostaining of 4 µm-thick tissue sections was performed and counterstained lightly with Carazzi's hematoxylin. The following primary antibodies were used: α-GFAP rabbit polyclonal (1:1000; DAKO), α-Tau AT100 mouse monoclonal (1:100; Invitrogen), α-alpha-Synuclein mouse monoclonal (1:40; Novocastra), α-beta-Amyloid mouse monoclonal (1:40; DAKO), α-Neurofilament mouse monoclonal (1:2000; Sternberger), α-Tau-3-repeat isoform RD3(1:3000; Millipore) and α-Tau-4 repeat isoform RD4 (1:100; Millipore). Primary antibody binding was detected by the labelled streptavidin-biotin method (DAKO; EnVision +System-HRP Labelled Polymer α-mouse) following the manufacturer's protocols.

Next-generation sequencing (NGS) panels and multiplex ligation-dependent probe amplification (MLPA) analysis

We designed a targeted NGS panel including the coding regions of 63 genes of PD, atypical Parkinsonism, Mendelian conditions that can cause Parkinsonism, and risk factors based on the evidence curated in the Mendelian Inheritance in Man (MIM) and the Movement Disorders Society Taskforce gene list[33] (Table S1).

CES was performed on the index case. Based on fragmentation and capture, exonic regions were enriched using Agilent® Technologies (Santa Clara, CA, USA). Agilent Technologies' CES panel includes 5833 genes in total. This step was needed to discard gene variants related to tau pathologies[34] (Table S4). The libraries obtained with the Nextera Rapid Captura Enrichment Kit (Illumina, San Diego, CA) were loaded on an Illumina MiniSeq system (Illumina) according to the manufacturer's instructions.

Bioinformatics analysis of NGS data was conducted using a homemade pipeline developed at the Bioinformatics Unit of the Molecular Genetics Department at the Sant Joan de Déu Hospital (Barcelona, Spain) as described previously[35]. All variants selected (MAF < 1%) were confirmed by Sanger sequencing and categorised according to the international guidelines of the American College of Medical Genetics and Genomics (ACMG)[36].

MLPA was used to identify copy number variations (CNVs) using the kit P051-D1 (MRC-Holland, Amsterdam, The Netherlands).

GBA1 deletion study

A *GBA1* CNV study was performed using long PCR, as previously described[37]. Amplicons were visualised in a 1% agarose gel and purified using the PureLink™ PCR Purification Kit (ThermoFisher, Waltham, MA, USA) following the manufacturer's protocol. The recovered DNA was Sanger sequenced.

Constructions of *LRRK2* expression plasmids

The pDEST53-$LRRK2^{WT}$ plasmid was a gift from the Mark Cookson Lab (#25044, Addgene). To generate the pDEST53-$LRRK2^{Leu119Pro;Leu488Pro}$ plasmid, the fragment of interest was excised from pDEST53-$LRRK2^{WT}$, cutting with *Xba*I (Thermo Fisher Scientific) and *Xho*I (Thermo Fisher Scientific) restriction enzymes. This fragment was cloned using T4 DNA ligase (Thermo Fisher Scientific) in the pBlueScript II SK plasmid (#212205, Addgene) previously digested with the same enzymes. Afterwards, we performed the double site-directed mutagenesis of the recombinant pBlueScript II SK by using the Q5® Site-Directed Mutagenesis kit (New England Biolabs). After each mutagenesis, Sanger sequencing with specific primers of the recombinant pBlueScript II SK mutant was needed to check the nucleotide change. The double mutant fragment containing the c.356 T > C and c.1463 T > C (for p.[Leu.119Pro; Leu488Pro]) nucleotide changes was excised with *Xba*I and *Xho*I and subcloned in pDEST53-$LRRK2^{WT}$ previously cut with the same enzymes. After ligation and selection, Sanger sequencing was carried out to check the *LRRK2* open reading frame (ORF) sequence.

Functional impact study of the new *LRRK2* allele

Transient transfection of constructs in the HEK293 cell line was performed using FuGENE® HD (Promega). After, cells were incubated at 37 °C for 48 h. The study of recombinant LRRK2 expression was in fixed cells with 4% paraformaldehyde and mounting medium Fluoromount-G with DAPI (4',6-diamidino-2-phenylindole) (Thermo Fisher Scientific). To evaluate

recombinant LRRK2 interactions with endogenous RAB8A and RAB10, we used Protein Ligation Assay (PLA, Duolink® In situ Detection Red Starter [Mouse/Rabbit] Kit, Sigma-Aldrich) and the following antibodies: mouse α-GFP (1:500; #ab1218), rabbit α-GFP (1:500; #ab6556), rabbit α-RAB8A (1:100; #ab188574) and mouse α-RAB10 (1:100; #SAB5300028).

We acquired the images using a Leica TCS SP8 X White Light Laser confocal microscope using a 63× oil immersion objective. Z-stacks were acquired every 0.1 µm along with the cell thickness. Image analysis was performed using maximum intensity projection in Image J/Fiji software (NIH, U.S.A. National Institutes of Health, Bethesda, MD, United States).

In silico protein structure preparation

We used PDB 5SZI for RAB8A and PDB 5LPN for RAB10, and computed the homology model of the LRRK2 ARM region (residues 12–650) using PDB 8FO2 as a template and the SWISS Homology model tool (https://swissmodel.expasy.org/). To obtain the LRRK2$^{Leu119Pro\text{-}Leu488Pro}$ variant structure, we first mutated the two residues using Maestro (Schrödinger Inc.) and equilibrated the system with a short molecular dynamics simulation. Briefly, using Gromacs v2023.31[38] and the AMBER99sb force field, we solvated a periodic cubic box consisting of TIP3 water model and Na^+ and Cl^- ions at 0.1 M/L. Then, we ran a steepest descent minimisation followed by 200 pico-seconds of constant number-volume-temperature (NVT) equilibration step of the water solvent, both with the LRRK2-ARM domain and ions restrained. Afterwards, to heat the system to 300 K, we ran a series of 10–50 ps of constant number-pressure-temperature (NPT) MD simulations using different LRRK2 residues constraints, with force constants of 1000 kJ/mol nm^2, 550 kJ/mol nm^2, 300 kJ/mol nm^2, 170 kJ/mol nm^2, 90 kJ/mol nm^2, 50 kJ/mol nm^2, 30 kJ/mol nm^2, 15 kJ/mol nm^2, 10 kJ/mol nm^2, and 5 kJ/mol nm^2. We then set up a production MD of 60 ns, using a 2 fs time step (300 K, 1 bar, particle-mesh Ewald for electrostatic interactions). The last snapshot of the simulation was used as the reference structure for the LRRK2$^{Leu119Pro;Leu488Pro}$ ARM region of the protein. Importantly, such short molecular dynamics allow accommodating non-local structural changes that might result from the p.Leu119Pro and p.Leu488Pro, changing the affinity and docking profiles along the ARM region, and not only locally.

Effect of p.[Leu119Pro;Leu488Pro] on the docking between LRRK2 and RAB

We ran two orthogonal analyses to measure the effect of both p.Leu119Pro and p.Leu488Pro on the docking between LRRK2 and RAB8A or RAB10. We used the Masif site[39], on the LRRK2-ARM structure, to generate a surface mesh, and compute its vertex-wise probability score that summarises the potential to interact with any other protein. We compare LRRK2^{WT} and LRRK2$^{Leu119Pro;Leu488Pro}$ scores for the vertices around residues 119 and 488 (5 Ams radius). Additionally, we used pyDock[40,41], a rigid docking software that generates around 92000 LRRK2-RAB complex poses (for both LRRK2^{WT} and LRRK2$^{Leu119Pro;Leu488Pro}$). We scored their binding affinity using a coarse-grained energy function. We then compared the number of LRRK2-RAB complexes within the top 100 and top 1000 energy scores, that are close (radius of 5A) to residue 119, residue 488, and residue 301 (top pyDock pose). This approach has previously shown that mutations at the interface and their effect on the number of top poses predicted by pyDock are related to missense variants[41]. Importantly, we run the same docking protocol between LRKK2 and RAB29 to compare its performance against a known crystal structure (PDB: 8ORF2). Among the top 60 pyDock energy-ranked conformations, we identified a pose with a DockQ score of 0.62, which is classified as medium quality according to CAPRI criteria. The ligand RMSD for this pose was 1.66 Å compared to the 8ORF2 PDB complex (Fig. S5), suggesting the reliability of pyDock for LRKK2-RAB systems.

Effect of p.[Leu119Pro;Leu488Pro] on interaction affinity between LRRK2 and RAB

To study interaction affinity, we first ran PELE[16], a heuristic MonteCarlo (MC) sampling method to characterise intermolecular interactions. Each MC step involves multiple events, including protein backbone perturbation (using anisotropic network models), side chain sampling and minimisation, all using the OPLS2005 force field. In brief, we selected all pyDock poses close to residue 119 and residue 301 (top pyDock pose) for both LRRK2^{WT} and LRRK2$^{Leu119Pro;Leu488Pro}$. We excluded residue 488 for further analyses, given the low score from Masif and the low number of top 100 poses from pyDock. Then, we used PROPKA 3.0 to calculate the protonation state of titratable residues at pH 7.4 for every complex pose. Right after, we ran PELE with an equilibration protocol (moving RAB with a rotation factor of 0.01 rad and translation range of 0.02 Å for 40 PELE MC steps using 30 independent trajectories) to correct interface clashes derived from pyDock predictions. Next, we selected the top 10 poses from the equilibration step and ran a production protocol (rotation factor of 0.01 or 0.05 rad, translation range of 0.05 or 0.4 Å, for 40 PELE MC steps and 100 independent trajectories) and computed the whole complex and the protein–protein interaction energies. Thereafter, we compared the energy profiles between LRRK2^{WT} and LRRK2$^{Leu119Pro;Leu488Pro}$.

Additionally, we used Steered Molecular Dynamics (SMD) as a second modelling tool. In brief, SMD is a set of non-equilibrium pulling simulations that apply specific work with a constant velocity to the system. SMD allows the comparison of the required work/force to accomplish the dissociation between LRRK2 and RAB8A or RAB10 for both LRRK2^{WT} and LRRK2$^{Leu119Pro;Leu488Pro}$. We first selected the top energy pyDock pose close to residue 119, and the top pyDock pose from LRRK2^{WT} to avoid biasing the results in favour of LRRK2$^{Leu119Pro;Leu488Pro}$. We then mutated p.Leu119Pro and p.Leu488Pro using Maestro and energy-minimised the system following the aforementioned MD pipeline. Thereafter, we ran 30 replicas of SMD using an umbrella potential along the direction of the vector between the centre of mass of RAB and the interface residues from LRRK2. Concretely, we used a force constant of 1000 kJ mol^{-1} nm^{-2}, a rate of change of 0.2 Å/ps, and restrained all the residues from LRRK2 during a total production time of 250 ps. We then compared the work profile between LRRK2^{WT} and LRRK2$^{Leu119Pro;Leu488Pro}$.

Statistical analysis

All data are expressed as means ± SD or box plots, showing the median. Box edges represent the 25th and 75th percentiles, and the whiskers extend to the minimum and maximum values. *P*-values are indicated by asterisks: $^*P$-value < 0.05.

Cochran–Mantel–Haenszel χ^2 test was performed for potential differences in mean percentages of pDEST53-LRRK2^{WT} and pDEST53-LRRK2$^{Leu119Pro;Leu488Pro}$ subcellular pattern localisation. The data's normality was assessed by the Shapiro test, followed by the student's *t*-test, considering whether the variances were equal or different.

Statistical computing was done using RStudio software version 1.2.1335, and graphs were created with GraphPad Prism version 8.0.1.

Data availability

All relevant data that support the findings of this study are presented in the main text and supplementary information. Other source data are available from the corresponding author upon reasonable request.

Received: 6 November 2024; Accepted: 2 May 2025;
Published online: 07 June 2025

References

1. Kluss, J. H., Mamais, A. & Cookson, M. R. LRRK2 links genetic and sporadic Parkinson's disease. *Biochem. Soc. Trans.* **47**, 651–661 (2019).
2. Ito, G., Tomita, T. & Utsunomiya-Tate, N. LRRK2-mediated phosphorylation and thermal stability of Rab12 are regulated by bound nucleotides. *Biochem. Biophys. Res. Commun.* **667**, 43–49 (2023).
3. Sosero, Y. L. & Gan-Or, Z. LRRK2 and Parkinson's disease: from genetics to targeted therapy. *Ann. Clin. Transl. Neurol.* **10**, 850–864 (2023).

4. Steger, M. et al. Phosphoproteomics reveals that Parkinson's disease kinase LRRK2 regulates a subset of Rab GTPases. *Elife* **5**, e12813 (2016).
5. Pfeffer, S. R. LRRK2 phosphorylation of Rab GTPases in Parkinson's disease. *FEBS Lett.* **597**, 811–818 (2023).
6. Steger, M. et al. Systematic proteomic analysis of LRRK2-mediated Rab GTPase phosphorylation establishes a connection to ciliogenesis. *Elife* **6**, e31012 (2017).
7. Waschbusch, D. et al. Structural basis for Rab8a recruitment of RILPL2 via LRRK2 phosphorylation of switch 2. *Structure* **28**, 406–417 e406 (2020).
8. Vides, E. G. et al. A feed-forward pathway drives LRRK2 kinase membrane recruitment and activation. *Elife* **11**, e79771 (2022).
9. Coku, I. et al. Functional analyses of two novel LRRK2 pathogenic variants in familial Parkinson's disease. *Mov. Disord.* **37**, 1761–1767 (2022).
10. Marchand, A., Drouyer, M., Sarchione, A., Chartier-Harlin, M. C. & Taymans, J. M. LRRK2 phosphorylation, more than an epiphenomenon. *Front Neurosci.* **14**, 527 (2020).
11. Hyman, B. T. et al. National Institute on aging-Alzheimer's Association guidelines for the neuropathologic assessment of Alzheimer's disease. *Alzheimers Dement* **8**, 1–13 (2012).
12. Iwaki, H. et al. Accelerating medicines partnership: Parkinson's disease. Genetic resource. *Mov. Disord.* **36**, 1795–1804 (2021).
13. Schrödinger, L. L. C. *The PyMOL Molecular Graphics System, Version 1.8* (Scientific Research, 2015).
14. Rodrigues, C. H. M., Pires, D. E. V. & Ascher, D. B. DynaMut2: Assessing changes in stability and flexibility upon single and multiple point missense mutations. *Protein Sci.* **30**, 60–69 (2021).
15. McGrath, E., Waschbusch, D., Baker, B. M. & Khan, A. R. LRRK2 binds to the Rab32 subfamily in a GTP-dependent manner via its armadillo domain. *Small GTPases* **12**, 133–146 (2021).
16. Borrelli, K. W., Vitalis, A., Alcantara, R. & Guallar, V. PELE: protein energy landscape exploration. A novel Monte Carlo based technique. *J. Chem. Theory Comput.* **1**, 1304–1311 (2005).
17. Melachroinou, K. et al. Activation of FADD-dependent neuronal death pathways as a predictor of pathogenicity for LRRK2 mutations. *PLoS One* **11**, e0166053 (2016).
18. Marku, A. et al. The LRRK2 N-terminal domain influences vesicle trafficking: impact of the E193K variant. *Sci. Rep.* **10**, 3799 (2020).
19. Kalogeropulou, A. F. et al. Impact of 100 LRRK2 variants linked to Parkinson's disease on kinase activity and microtubule binding. *Biochem. J.* **479**, 1759–1783 (2022).
20. Vieweg, S. et al. PINK1-dependent phosphorylation of Serine111 within the SF3 motif of Rab GTPases impairs effector interactions and LRRK2-mediated phosphorylation at Threonine72. *Biochem. J.* **477**, 1651–1668 (2020).
21. Yin, G. et al. alpha-Synuclein interacts with the switch region of Rab8a in a Ser129 phosphorylation-dependent manner. *Neurobiol. Dis.* **70**, 149–161 (2014).
22. Bonet-Ponce, L. et al. LRRK2 mediates tubulation and vesicle sorting from lysosomes. *Sci. Adv.* **6**, eabb2454 (2020).
23. Eguchi, T. et al. LRRK2 and its substrate Rab GTPases are sequentially targeted onto stressed lysosomes and maintain their homeostasis. *Proc. Natl. Acad. Sci. USA* **115**, E9115–E9124 (2018).
24. Mamais, A. et al. Mutations in LRRK2 linked to Parkinson disease sequester Rab8a to damaged lysosomes and regulate transferrin-mediated iron uptake in microglia. *PLoS Biol.* **19**, e3001480 (2021).
25. Mamais, A. et al. The LRRK2 kinase substrates RAB8a and RAB10 contribute complementary but distinct disease-relevant phenotypes in human neurons. *Stem Cell Rep.* **19**, 163–173 (2024).
26. Bandres-Ciga, S. et al. Genome-wide assessment of Parkinson's disease in a Southern Spanish population. *Neurobiol. Aging* **45**, 213 e213–213 e219 (2016).
27. Ichinose, Y. et al. Neuroimaging, genetic, and enzymatic study in a Japanese family with a GBA gross deletion. *Parkinsonism Relat. Disord.* **61**, 57–63 (2019).
28. Henderson, M. X., Sengupta, M., Trojanowski, J. Q. & Lee, V. M. Y. Alzheimer's disease tau is a prominent pathology in LRRK2 Parkinson's disease. *Acta Neuropathol. Commun.* **7**, 183 (2019).
29. Hughes, A. J., Daniel, S. E., Kilford, L. & Lees, A. J. Accuracy of clinical diagnosis of idiopathic Parkinson's disease: a clinico-pathological study of 100 cases. *J. Neurol. Neurosurg. Psychiatry* **55**, 181–184 (1992).
30. Fahn, S. & Elton, R. L. *Unified Parkinson's disease rating scale* (Macmillan Healthcare Information, Flor-ham Park, 1987).
31. Hoehn, M. M. & Yahr, M. D. Parkinsonism: onset, progression and mortality. *Neurology* **17**, 427–442 (1967).
32. Emre, M., et al. Clinical diagnostic criteria for dementia associated with Parkinson's disease. *Mov. Disord.* **22**, 1689–1707 (2007).
33. Marras, C. et al. Nomenclature of genetic movement disorders: Recommendations of the International Parkinson and Movement Disorder Society task force. *Mov. Disord.* **32**, 724–725 (2017).
34. Tacik, P., Sanchez-Contreras, M., Rademakers, R., Dickson, D. W. & Wszolek, Z. K. Genetic disorders with tau pathology: a review of the literature and report of two patients with tauopathy and positive family histories. *Neurodegener. Dis.* **16**, 12–21 (2016).
35. Natera-de Benito, D. et al. Common pathophysiology for ANXA11 disorders caused by aspartate 40 variants. *Ann. Clin. Transl. Neurol.* **10**, 408–425 (2023).
36. Richards, S. et al. Standards and guidelines for the interpretation of sequence variants: a joint consensus recommendation of the American College of Medical Genetics and Genomics and the Association for Molecular Pathology. *Genet Med* **17**, 405–424 (2015).
37. Siebert, M. et al. Novel mutations in the glucocerebrosidase gene of Brazilian patients with Gaucher disease. *JIMD Rep.* **9**, 7–16 (2013).
38. Abraham, M. et al. *GROMACS 2023.3 Source Code* (GROMACS, 2023).
39. Gainza, P. et al. Deciphering interaction fingerprints from protein molecular surfaces using geometric deep learning. *Nat. Methods* **17**, 184–192 (2020).
40. Cheng, T. M., Blundell, T. L. & Fernandez-Recio, J. pyDock: electrostatics and desolvation for effective scoring of rigid-body protein–protein docking. *Proteins* **68**, 503–515 (2007).
41. Barradas-Bautista, D. & Fernandez-Recio, J. Docking-based modeling of protein–protein interfaces for extensive structural and functional characterization of missense mutations. *PLoS One* **12**, e0183643 (2017).

Acknowledgements

We thank the family for participating in this study. We are indebted to Jordi Pijuan and Teresa Periñan Tocino for their invaluable assistance with the in silico analyses and data regarding variant frequencies in PD populations, respectively. This study has been funded by Instituto de Salud Carlos III (ISCIII) through the project "PI22/00680" [J.H.] and co-funded by the European Union; the AGAUR/Generalitat de Catalunya and European Regional Development Fund (FEDER), (Grants SLT002/16/0030, 2021-SGR-01610 [F.P.]) and Juan de La Cierva JDC2022-048942-I from the Ministerio de Ciencia e Innovación. The funders played no role in study design, data collection, analysis and interpretation of data, or the writing of this manuscript. Data on variant frequencies in PD populations were obtained in April 2025 from the AMP-PD. The CIBERER is an initiative of the Instituto de Salud Carlos III and the Department of Genetic Medicine of Sant Joan de Déu Children's Hospital is part of the 'Centre Daniel Bravo de Diagnòstic i Recerca de Malalties Minoritàries'.

Author contributions

L.V.-D. studied and interpreted the family clinical and genetics data. C.G. performed and interpreted the neuropathology study. A.P. performed genetic and cellular studies. M.O.-L. performed genetic studies. V.M. and V.G. performed and interpreted docking analysis. J.H. provided funding. J.H. and F.P. conceptualised work and wrote the first draft. All authors contributed, read and approved the final manuscript.

Competing interests
The authors declare no competing interests.

Additional information
Supplementary information The online version contains supplementary material available at https://doi.org/10.1038/s41531-025-00989-y.

Correspondence and requests for materials should be addressed to Janet Hoenicka.